Polymer lattices as mechanically tunable 3-dimensional photonic crystals operating in the infrared

V. F. Chernow, H. Alaeian, J. A. Dionne, and J. R. Greer

Articles you may be interested in

Semicrystalline woodpile photonic crystals without complicated alignment via soft lithography
Appl. Phys. Lett. **96**, 193303 (2010); 10.1063/1.3425756

Mechanical properties and tuning of three-dimensional polymeric photonic crystals
Appl. Phys. Lett. **91**, 241904 (2007); 10.1063/1.2822825

Tunable defect mode in a three-dimensional photonic crystal
Appl. Phys. Lett. **87**, 241108 (2005); 10.1063/1.2139846

Tunable electrochromic photonic crystals
Appl. Phys. Lett. **86**, 221110 (2005); 10.1063/1.1929079

Mechanically tunable photonic crystal structure
Appl. Phys. Lett. **85**, 4845 (2004); 10.1063/1.1823019

Polymer lattices as mechanically tunable 3-dimensional photonic crystals operating in the infrared

V. F. Chernow,[1,a)] H. Alaeian,[2,3] J. A. Dionne,[3] and J. R. Greer[1,4]

[1]*Division of Engineering and Applied Sciences, California Institute of Technology, Pasadena, California 91125, USA*
[2]*Department of Electrical Engineering, Stanford University, Stanford, California 94305, USA*
[3]*Department of Materials Science and Engineering, Stanford University, Stanford, California 94305, USA*
[4]*The Kavli Nanoscience Institute, California Institute of Technology, Pasadena, California 91125, USA*

Broadly tunable photonic crystals in the near- to mid-infrared region could find use in spectroscopy, non-invasive medical diagnosis, chemical and biological sensing, and military applications, but so far have not been widely realized. We report the fabrication and characterization of three-dimensional tunable photonic crystals composed of polymer nanolattices with an octahedron unit-cell geometry. These photonic crystals exhibit a strong peak in reflection in the mid-infrared that shifts substantially and reversibly with application of compressive uniaxial strain. A strain of ∼40% results in a 2.2 μm wavelength shift in the pseudo-stop band, from 7.3 μm for the as-fabricated nanolattice to 5.1 μm when strained. We found a linear relationship between the overall compressive strain in the photonic crystal and the resulting stopband shift, with a ∼50 nm blueshift in the reflection peak position per percent increase in strain. These results suggest that architected nanolattices can serve as efficient three-dimensional mechanically tunable photonic crystals, providing a foundation for new opto-mechanical components and devices across infrared and possibly visible frequencies. © 2015 AIP Publishing LLC. [http://dx.doi.org/10.1063/1.4930819]

Three-dimensional (3D) photonic crystals (PhCs) have been the focus of ever-increasing interest in the scientific community given their potential to impact areas spanning energy conversion to analyte sensing. These architected materials have a periodic variation in their refractive index and selectively reflect light of wavelengths on the order of their periodicity.[1] Though only a few 3D PhCs possess a complete photonic bandgap,[2,3] defined as a range of frequencies for which incident light cannot propagate in any direction, all 3D PhCs have stopbands that forbid light propagation in some crystallographic directions.[4] Within the spectral range of a photonic bandgap or stopband, light is selectively reflected, rendering 3D PhCs applicable in numerous optical devices such as low-loss mirrors,[5,6] lasers,[7] chemical[8] and mechanical[9,10] sensors, and displays.[11–13] Several of these applications, including variable filters, laser sources, and strain sensors,[4] require that the PhC be reconfigurable or reversibly tunable while maintaining structural integrity, which would enable them to be optically active over a wide range of frequencies. Most existing fabrication methodologies produce PhCs that operate over a fixed and limited bandwidth.[14] The response of these otherwise passive PhCs can be rendered active by fabricating structures using dynamic materials which can respond to external stimuli including, for example, electric fields, solvent swelling, and mechanical deformation.

Stopband position can be tuned by changing either the refractive index and/or the periodicity of the PhC structure, with the latter being generally more straightforward.[15] The number of experimentally available methods for modulating the lattice periodicity exceeds the number of index-tunable materials, and, more importantly, altering the lattice constant often leads to a more substantial stopband shift.[16,17] Several approaches that can reversibly tune the stopband position of PhCs post-fabrication—for example, methods based on temperature gradients,[18,19] electric fields,[20,21] and solvent swelling[22]—often suffer from limited tuning ranges, typically restricted to between 100 and 200 nm shifts. Compositional or structural changes that arise within 3D PhCs in response to mechanical deformation allow for wider tuning ranges, but are sometimes irreversible.[23,24] In addition, most of the existing mechanically tunable 3D PhCs have been limited to opal and inverse opal type structures.[4,16,23,24]

We fabricated 3-dimensional polymer nanolattices with ∼4 μm wide octahedron unit cells that act as PhCs and can be stably and reversibly tuned by mechanical compression over multiple cycles. The mechanical properties of similarly architected hollow metallic and ceramic octahedron nanolattices have been reported.[25–27] In this work, the polymeric composition facilitates maximum optical tunability and reversibility. We find that a reversible ∼2.2 μm stopband blueshift can be achieved with a uniaxial compression of ∼40% and that the blueshift is linear for applied strains from 0% to 40%.

To fabricate the nanolattices, we used the direct laser writing (DLW) two-photon lithography (TPL) system, Photonic Professional (Nanoscribe GmbH, Germany). Samples were prepared by drop-casting the negative-tone photoresist "IP-Dip" (Nanoscribe GmbH) on a 500 μm thick polished silicon substrate; "IP-Dip" photoresist is composed primarily (>95%) of the monomer pentaerythritol triacrylate. An infrared laser was then used to crosslink and write a preprogrammed pattern into the acrylic-based photopolymer via two-photon absorption. The exposed sample was then

a)Author to whom correspondence should be addressed. Electronic mail: vchernow@caltech.edu.

107, 101905-1

developed for 30 min in propylene glycol monomethyl ether acetate and isopropanol. This process allows for maximum control over the final architecture and enables the fabrication of arbitrarily complex nano- and micro-structures. Figure 1(a) shows that the nanolattices have individual octahedron unit cells on the order of ∼4 μm and are 6.5 unit cells tall. Individual beams have elliptical cross-sections, with short axes of ∼500 nm and long axes of ∼1.75 μm.

Mechanical characterization of the nanolattices was performed using an *in-situ* nanoindentation system, InSEM (Nanomechanics Inc.), inside an SEM chamber (see Ref. 28 for specifications). This instrument enables precise measurement of applied load vs. displacement data with simultaneous real-time visualization of nanolattice deformation.[28] *In-situ* uniaxial compression experiments were conducted at a constant prescribed displacement rate of 50 nm/s. Nanolattices were aligned orthogonal to the electron-beam and in line with the nanoindenter arm, such that the periodicity of the lattice was gradually reduced along this compression axis.

Samples were strained by >60% before reaching the instrument load limit of 35 mN. Figure 1(b) shows representative stress-strain data and SEM micrographs captured at various points during a typical experiment. It appears that the polymer nanolattices underwent a global compression, where each layer of unit cells was compressed in a homogenous fashion, gradually decreasing the pitch of the structure. This is in contrast to a layer-by-layer collapse mechanism typical of hollow ceramic and metallic octahedron nanolattices.[25–27] It also appears that the Poisson's ratio of the nanolattices is close to zero because no transverse deformation was observed—the structure neither expanded nor contracted

laterally—in response to axial strain. This behavior is likely due to the fact that compressive straining will cause beams to buckle into the pores of the lattice structure, instead of contributing to lateral expansion or contraction. Analysis of SEM images and a hysteresis in the stress-strain data revealed that the structure recovered by ∼82% nearly immediately following load removal after compression in excess of 60%. The acrylic-based polymer that comprises the nanolattice is viscoelastic and continues to recover with time through a time-dependent strain response. We observed a recovery to ∼90% of the original height within hours of the primary compression. Subsequent to the initial cycle of compression and recovery, samples were compressed again to $\varepsilon \sim 60\%$ and appeared to recover to ∼100% of their initially recovered height after this second cycle. Lattices were compressed to $\varepsilon \sim 60\%$ a 3rd and 4th time and showed similar recovery. This result suggests that a few permanent structural defects were formed during the initial compression, and for all subsequent deformations, the structure acts elastically and recovers completely and instantaneously.

The micron-scale unit cell size of the nanolattices suggests that the PhC will exhibit a bandgap in the infrared range. We used Fourier Transform Infrared (FTIR) microspectroscopy to evaluate the optical properties of the nanolattices, including their reflectance and stopband position. Spectra were acquired using a Nicolet iS50 FT-IR spectrometer equipped with a Nicolet Continuum Infrared Microscope. For this particular setup, the angular range of incidence was 16°–35.5° relative to the normal.

To establish a baseline understanding of the relationship between strain and the position of the stop band, we fabricated several nanolattices which mimicked compressed morphologies for 4 strains—0%, 14.8%, 27.1%, and 38.6%—corresponding to unit cell angles of approximately 45°, 40°, 35°, and 30°, as shown in Figures 2(a) and 2(b). These "effectively strained" angle-varied nanolattices were fabricated with slightly altered geometries such that the unit cells evolved from fully isotropic in the unstrained state, to progressively more anisotropic at higher effective strains (Figure 2(b)). Increasing the degree of anisotropy in the unit cells also serves to uniformly decrease the height and periodicity of the overall lattice, with the effective strains calculated based on the relative change in the unit cell angle experienced by octahedron nanolattices during *in-situ* compression experiments. Compacting lattice periodicity along the z-direction by altering the unit cell angle allowed us to create a set of effectively strained lattices which represent idealized versions of the compressed octahedron PhC at 0%, 14.8%, 27.1%, and 38.6% strain.

Figure 2(c) shows the FTIR reflectance spectra for the four nanolattices. For the as-fabricated nanolattices, a significant peak in normalized reflectance emerges and is centered at 7.42 μm, which corresponds to the first order stop band. The center of this peak shifts to progressively shorter wavelengths for nanolattices with decreasing pitch: from 7.42 μm for the unstrained nanolattice to 6.40 μm for the 14.8% effectively strained nanolattice, to 5.38 μm for 27.1% effective strain, and to 4.61 μm for the 38.6% effectively strained sample. The plot in Figure 2(d) reveals the relationship between the central position of each stop band peak, denoted λ_{peak},
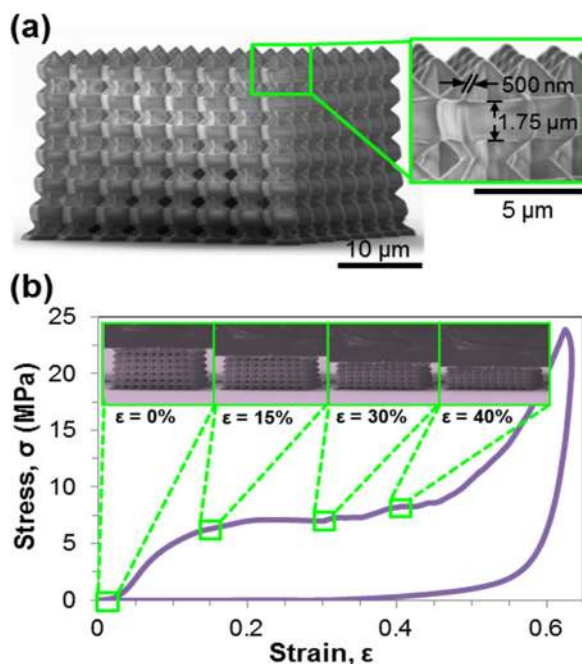

FIG. 1. (a) Scanning electron microscopy (SEM) images of a representative as-fabricated octahedron nanolattice. Inset shows relevant dimensions of the unit cell. (b) Representative stress-strain data for a uniaxial compression of an octahedron nanolattice. Inset images are scanning electron micrographs of the nanolattice, captured simultaneously at various points during the compression experiment.
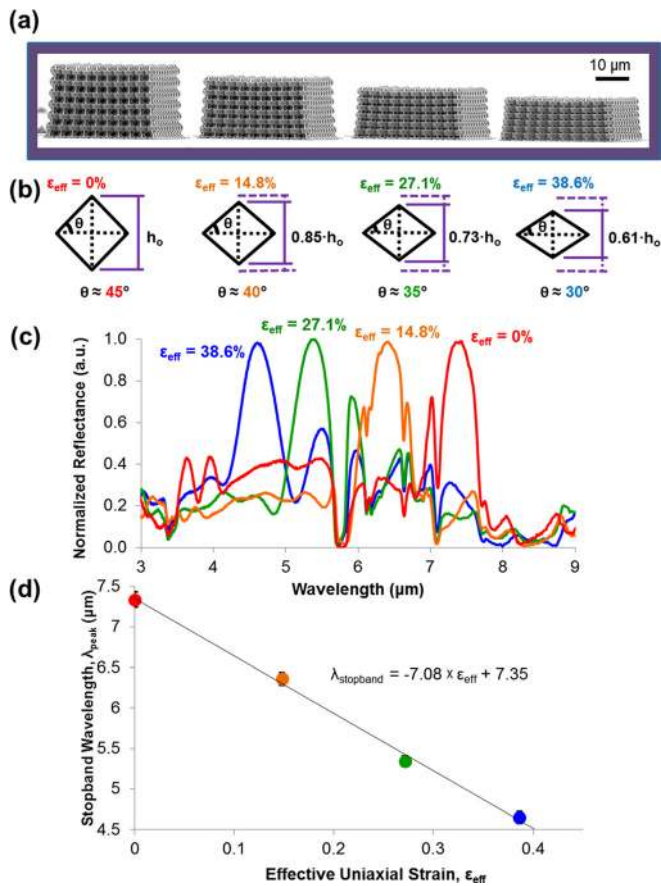
FIG. 2. (a) SEM images of octahedron nanolattices fabricated with varying angles, corresponding to different degrees of effective strain. (b) Schematic of the relationship between unit cell angle and effective strain in the fabricated nanolattice. (c) Normalized reflection spectra of a 45° unstrained octahedron nanolattice, and three angle-varied nanolattices, corresponding to increasing degrees of effective strain, ε_{eff}. (d) Effective strain-stopband plot for the angle-varied lattices. Note that ε_{eff} and λ_{peak} are directly proportional.
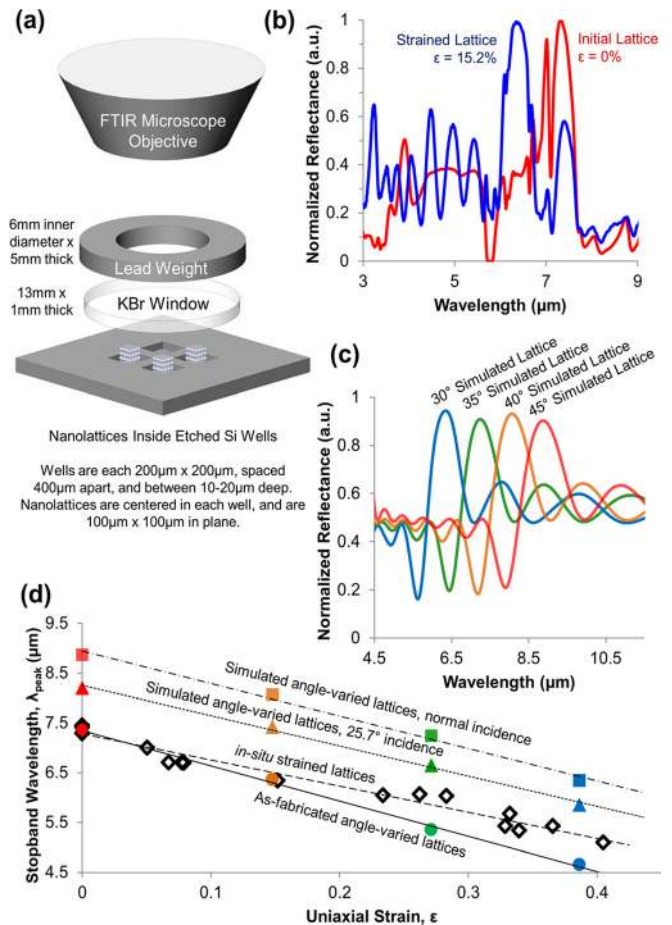

FIG. 3. (a) Schematic of the nanolattice compression cell setup. (b) Normalized reflectance spectra for an as-fabricated nanolattice outside of the compression cell (red), and under compression (blue) using the custom FTIR compression cell setup shown in (a). (c) Normalized reflection spectra under normal illumination for a simulated 45° unstrained octahedron nanolattice, and three simulated angle-varied nanolattices, each with corresponding degrees of increasing effective strain. The main peak for each simulated nanolattice corresponds to a 1st order Bragg reflection; secondary peaks that appear at longer wavelengths are caused by the higher order Bragg reflections. (d) Strain-stopband plots comparing data from the as-fabricated angle-varied lattices under corresponding effective strain, experimentally strained nanolattices using a compression cell over multiple cycles, and the simulated angle-varied lattices at normal incidence, and 25.7° incidence.

and effective strain, ε_{eff}, based on the normalized reflectance measurements of 24 separate unstrained and effectively strained samples (6 samples for each strain). In addition to the blueshifting of the photonic bandgap with increasing effective strain, the stopband data appear to vary linearly with strain. This is not unexpected because the opto-mechanical response of these 3D PhCs under uniaxial compression is associated with a change in spacing of closest-packed planes, and a consequent change in the Bragg resonance condition and peak wavelength. This trend is similar to the stopband-strain relationships reported for 1D and 2D mechanically tunable photonic crystals.[1,29] The largest stopband shift of 2.8 μm was exhibited by samples that were effectively strained by ~40%. This stopband shift is more substantial than the 1.25 μm shift achieved by solvent swelling of lamellar photonic crystal gels outlined by Kang *et al.*,[15] and outperforms other elastomeric 3D photonic crystals like the one reported by Fudouzi and Sawada where a 20% strain leads to a 30 nm stopband shift.[30]

The nearly full recoverability of the compressed polymeric nanolattices studied in this work required the design of a special experimental setup which could measure the optical response of compressed nanolattices in their strained state. Figure 3(a) provides a schematic of the custom compression

cell setup, which was constructed by first etching wells of varying depths into a silicon substrate using deep-reactive ion etching, followed by the fabrication of pristine unstrained nanolattices into individual wells. An IR-transparent KBr slide was then placed on top of the nanolattices and wells, and then, to ensure uniaxial straining of the lattices, a washer-shaped lead weight was placed on to the slide. Using this compression cell, it was possible to strain an as-fabricated sample to a preordained position and fix it in the strained state by bounding from above by the IR-transparent KBr slide, while it sits affixed to the polished Si substrate. We then collected reflectance with the same FT-IR spectrometer as used on the effectively strained samples. Four experiments on cyclically strained nanolattices were carried out, with each one corroborating the finding that compressing an octahedron nanolattice leads to a blueshifting in the PhC stopband, and releasing the load shifts the stopband back to within 89.8 ± 2.8% of the original stopband position

of the pristine nanolattice—a value commensurate with the ~90% recovery observed in nanolattice height following primary compression. Figure 3(b) shows the reflection spectrum of a representative sample. For this particular sample, the stopband of the initial nanolattice was centered at 7.32 μm and that of the 15.2% strained nanolattice blueshifted to 6.34 μm. For this series of strained nanolattice experiments, the applied strain was monitored by calculating the pathlength of the FTIR compression cell using interference fringes which appear in the background reflection spectra.[31] The KBr surface of the cell is positioned nearly parallel to the Si substrate—between which the nanolattices are sandwiched—which results in the appearance of sinusoidal fringes in the spectra. These fringes are created by interference between light that has been transmitted through the sample, and light that has been reflected internally between the parallel surfaces.[31] The number and the position of interference fringes allow us to estimate the pathlength through the compression cell,[31] which is equivalent to the thickness of the sample and the height of the compressed nanolattices

$$d = \frac{N\lambda_1\lambda_2}{2n_{eff}\cos\theta(\lambda_2 - \lambda_1)}.$$

Here, d is the sample thickness or compression cell pathlength, N is the number of interference fringes between the wavelength range λ_1 and λ_2, n_{eff} is the effective refractive index of the material within a well of the compression cell, and θ is the average angle of incident light on the sample. Having measured the height of pristine, unstrained nanolattices using SEM imaging, and calculated the cell pathlength for a compressed sample, we obtained a value for applied compressive strain. Full details on this analysis are provided in the supplementary material and in Figure S3.[32]

Figure 3(d) shows that *in-situ* straining of the nanolattices results in a blueshifting of the stopband and that a linear relationship holds between applied strain and stopband position. The slope of this linear dependency is a factor of 1.42 lower than the slope predicted by the idealized, effectively strained nanolattices, also plotted in Figure 3(d) for comparison. This plot reveals that nanolattices strained by 40.5% exhibited a stopband shift of 2.19 μm, compared to a 2.87 μm shift for the effectively strained angle-varied nanolattices compressed by the same amount. This plot also shows that, at high strains of $\varepsilon \sim 40\%$, the percent error between the measured λ_{peak} for *in-situ* strained and angle-varied lattices is 14.1%, while at low strains, on the order of $\varepsilon \sim 10\%$, the percent error is significantly smaller, at 1.7%. These deviations likely arise from minor shearing in the *in-situ* setup that accompanies the nominal uniaxial compressive straining of the lattice. Shear strain in this system may take the form of a torquing at the nodes of the unit cells comprising the lattice, which leads to a shape change rather than a volume change and does not affect the periodicity of the lattice in the vertical direction to the same degree predicted by the angle-varied lattices modelling effective strain. It has been previously shown that the stopband position increases nonlinearly with shear strain,[1] which may also contribute to our observation of larger deviations from the λ_{peak} position

of the angle-varied lattices modelling effective strain, where only uniaxial strain was taken into account.

Despite the slight differences between the *in-situ* strained and as-fabricated effectively strained lattice spectra, these experimental results appear to agree well with numerical calculations. Figure 3(c) shows full-field Finite Difference Time Domain (FDTD) simulations of the reflectance from angle-varied nanolattices. The simulated geometries were determined by using SEM images of the fabricated experimental samples; the polymer refractive index of n $\sim$ 1.5 was determined by fitting FTIR reflectance data for TPL polymerized IP-Dip thin films using a scattering matrix approach combined with a minimization technique (see supplementary material for a more complete discussion).[32] IR-VASE ellipsometry would have been the preferred method for determining the refractive index of IP-Dip, but, since this resist is designed to be drop cast and polymerized using two-photon absorption, spin coated and UV-flood exposed samples did not possess the film uniformity or crosslinking density necessary to obtain accurate index measurements with this technique.

For the FDTD simulations, nanolattices were assumed to reside on an infinite slab of Si with a fixed refractive index of 3.4 over all frequencies. Figure 3(c) shows the reflectance spectra for four different simulated angle-varied octahedron unit cells, 45°, 40°, 35°, and 30°, illuminated with a normal-incidence plane wave. The simulations show a clear blueshift of the reflection peak with decreasing apex angle of the octahedron unit cell, in agreement with experimental results. These numerical results also display a linear trend between reflection peak position and effective strain, as do the experiments on the as-fabricated and *in-situ* strained nanolattices (see Figure 3(d)). Despite the difference in the actual position of λ_{peak} for the fabricated and simulated angle-varied lattices, the slopes of these lines are very similar. While the simulations appear to over-predict the stopband wavelength, this discrepancy in λ_{peak} position is in large part due to the angle of incident light used for illuminating simulated and fabricated samples; simulated samples are illuminated using plane waves incident at a single angle, and fabricated samples are under illumination from a Gaussian beam with an angular range between 16° and 35.5°. Simulating nanolattices at an average illumination angle of 25.7° does shift the calculated stopband peak closer to the experimentally measured peaks. Further discrepancies can be attributed to some non-idealities in the fabricated samples like the imperfect uniformity of beams and unit cells, and buckling at the joints between unit cells.

The reflection peak observed in our experiments and simulations can be attributed to the 1st order Bragg reflection in the lattice. Bragg's law is formulated as $2d \times \cos\theta = n\lambda$, where d is the vertical separation between two layers in the lattice, θ is the angle of the incident beam with the normal line, and n is the order of the Bragg reflection. A monotonic decrease in d from uniaxial strain will result in a monotonic decrease in the resonance wavelength λ_{peak}. This result is in agreement with the general blueshift trend observed both in the numerical and experimental data. Additional reflection peaks observed at longer wavelengths can be attributed to higher orders of the Bragg grating and are substantially

weaker than the main peak of the lattice. More details regarding the lattice band structure, as well as variation in the primary resonance peak with the incident angle, can be found in the supplementary material.[32]

This work demonstrates fabrication and characterization methodologies for 3-dimensional polymer nanolattices, active in the mid-IR range, whose photonic bandgap can be reversibly modulated as a function of uniaxial compressive strain. Opto-mechanical experiments and theory reveal that applied uniaxial compressive strain and the photonic stop-band are linearly related, with a maximum attained bandgap shift of $\sim$2.2 μm at $\sim$40% compressive strain. These findings imply that architected nanolattices may be utilized for emerging applications including but not limited to optical strain gauges, accelerometer, and other mechanical sensors, as well as tunable laser sources and variable filters. And while 3D lattice fabrication using TPL DLW is currently constrained by the minimum axial resolution attainable, restricting the dimensions of the octahedron geometry studied here to unit cell sizes of no less than 2.5 μm, advances like stimulated-emission-depletion (STED) DLW are pushing the resolution limits of this technology and may soon enable the patterning of any arbitrary 3D lattice with photonic properties extended into the visible range.

[1]E. P. Chan, J. J. Walish, A. M. Urbas, and E. L. Thomas, Adv. Mater. **25**, 3934 (2013).

[2]A. Blanco, E. Chomski, S. Grabtchak, M. Ibisate, S. John, S. Leonard, C. Lopez, F. Meseguer, H. Miguez, J. Mondia, G. Ozin, O. Toader, and H. M. van Driel, Nature **405**, 437 (2000).

[3]S. Noda, K. Tomoda, N. Yamamoto, and A. Chutinan, Science **289**, 604 (2000).

[4]A. C. Arsenault, T. J. Clark, G. von Freymann, L. Cademartiri, R. Sapienza, J. Bertolotti, E. Vekris, S. Wong, V. Kitaev, I. Manners, R. Z. Wang, S. John, D. Wiersma, and G. A. Ozin, Nat. Mater. **5**, 179 (2006).

[5]Y. Fink, J. N. Winn, S. Fan, C. Chen, J. Michel, J. D. Joannopoulos, and E. L. Thomas, Science **282**, 1679 (1998).

[6]S. D. Hart, G. R. Maskaly, B. Temelkuran, P. H. Prideaux, J. D. Joannopoulos, and Y. Fink, Science **296**, 510 (2002).

[7]J. Yoon, W. Lee, J. M. Caruge, M. Bawendi, E. L. Thomas, S. Kooi, and P. N. Prasad, Appl. Phys. Lett. **88**, 091102 (2006).

[8]M. Ben-Moshe, V. L. Alexeev, and S. A. Asher, Anal. Chem. **78**, 5149 (2006).

[9]L. M. Fortes, M. C. Gonçalves, and R. M. Almeida, Opt. Mater. (Amsterdam) **33**, 408 (2011).

[10]E. P. Chan, J. J. Walish, E. L. Thomas, and C. M. Stafford, Adv. Mater. **23**, 4702 (2011).

[11]A. C. Arsenault, D. P. Puzzo, I. Manners, and G. A. Ozin, Nat. Photonics **1**, 468 (2007).

[12]K. Hwang, D. Kwak, C. Kang, D. Kim, Y. Ahn, and Y. Kang, Angew. Chem., Int. Ed. **50**, 6311 (2011).

[13]Y. Lu, H. Xia, G. Zhang, and C. Wu, J. Mater. Chem. **19**, 5952 (2009).

[14]I. M. Pryce, K. Aydin, Y. A Kelaita, R. M. Briggs, and H. A Atwater, Nano Lett. **10**, 4222 (2010).

[15]Y. Kang, J. J. Walish, T. Gorishnyy, and E. L. Thomas, Nat. Mater. **6**, 957 (2007).

[16]M. G. Han, C. G. Shin, S.-J. Jeon, H. Shim, C.-J. Heo, H. Jin, J. W. Kim, and S. Lee, Adv. Mater. **24**, 6438 (2012).

[17]C. L. Yu, H. Kim, N. de Leon, I. W. Frank, J. T. Robinson, M. McCutcheon, M. Liu, M. D. Lukin, M. Loncar, and H. Park, Nano Lett. **13**, 248 (2013).

[18]K. Yoshino, Y. Shimoda, Y. Kawagishi, K. Nakayama, and M. Ozaki, Appl. Phys. Lett. **75**, 932 (1999).

[19]S. W. Leonard, J. P. Mondia, H. M. Van Driel, O. Toader, S. John, K. Busch, A. Birner, U. Gosele, and V. Lehmann, Phys. Rev. B **61**, R2389 (2000).

[20]J. Xia, Y. Ying, and S. H. Foulger, Adv. Mater. **17**, 2463 (2005).

[21]K. Busch and S. John, Phys. Rev. Lett. **83**, 967 (1999).

[22]H. Fudouzi and Y. Xia, Adv. Mater. **15**, 892 (2003).

[23]B. Viel, T. Ruhl, and G. P. Hellmann, Chem. Mater. **19**, 5673 (2007).

[24]K. Sumioka, H. Kayashima, and T. Tsutsui, Adv. Mater. **14**, 1284 (2002).

[25]L. C. Montemayor, L. R. Meza, and J. R. Greer, Adv. Eng. Mater. **16**, 184 (2014).

[26]D. Jang, L. R. Meza, F. Greer, and J. R. Greer, Nat. Mater. **12**, 893 (2013).

[27]L. R. Meza and J. R. Greer, J. Mater. Sci. **49**, 2496 (2014).

[28]J. Y. Kim and J. R. Greer, Acta Mater. **57**, 5245 (2009).

[29]W. Park and J.-B. Lee, Appl. Phys. Lett. **85**, 4845 (2004).

[30]H. Fudouzi and T. Sawada, Langmuir **22**, 1365 (2006).

[31]P. R. Griffiths and J. A. De Haseth, *Fourier Transform Infrared Spectroscopy*, 2nd ed. (John Wiley & Sons, Inc., 2007).

[32]See supplementary material at http://dx.doi.org/10.1063/1.4930819 for the fabrication of the compression cell, cell pathlength calculations, absorption features in FTIR spectra, polymer refractive index calculations, FDTD parameters for scattering and band diagrams, and simulation of stopband dependence on angle of incidence.